

Simulation of wave propagation in linear thermoelastic media

José M. Carcione¹, Zhi-Wei Wang², Wenchang Ling³, Ettore Salusti⁴, Jing Ba³, and Li-Yun Fu⁵

ABSTRACT

We have developed a numerical algorithm for simulation of wave propagation in linear thermoelastic media, based on a generalized Fourier law of heat transport in analogy with a Maxwell model of viscoelasticity. The wavefield is computed by using a grid method based on the Fourier differential operator and two time-integration algorithms to cross-check solutions. Because the presence of a slow quasistatic mode (the thermal mode) makes the differential equations stiff and unstable for explicit time-stepping methods, first, a second-order time-splitting algorithm solves the unstable part analytically and a Runge-Kutta method the regular equations. Alternatively, a first-order explicit Crank-

Nicolson algorithm yields more stable solutions for low values of the thermal conductivity. These time-stepping methods are second- and first-order accurate, respectively. The Fourier differential provides spectral accuracy in the calculation of the spatial derivatives. The model predicts three propagation modes, namely, a fast compressional or (elastic) P-wave, a slow thermal P diffusion/wave (the T-wave), having similar characteristics to the fast and slow P-waves of poroelasticity, respectively, and an S-wave. The thermal mode is diffusive for low values of the thermal conductivity and wave-like for high values of this property. Three velocities define the wavefront of the fast P-wave, i.e., the isothermal velocity in the uncoupled case, the adiabatic velocity at low frequencies, and a higher velocity at high frequencies.

INTRODUCTION

The theory of thermoelasticity combines that of heat conduction with the theory of elasticity; specifically, it describes the coupling between the fields of deformation and temperature. The theory is relevant for geophysical studies such as seismic attenuation (Zener, 1938; Treitel, 1959; Savage, 1966; Armstrong, 1984), geothermal exploration (e.g., Jacquey et al., 2015), and earthquake seismology (Boschi, 1973). Basically, a mechanical source of elastic waves induces a temperature field, whose heat flow equalizes the temperature difference with the surroundings giving rise to energy dissipation. On the other hand, a heat source generates viscoelastic waves.

Biot (1956), Deresiewicz (1957), Savage (1966), and Armstrong (1984) use the differential equations based on the Fourier law of heat conduction, but this formulation has unphysical solutions such

as discontinuities and infinite velocities as a function of frequency because it is based on a parabolic-type differential equation. A more general (physical) system of equations, based on a hyperbolic heat-transfer equation, has been analyzed in detail by Rudgers (1990) (the lattice model), which contains a relaxation term in the heat equation (Vernotte, 1948; Cattaneo, 1958), leading to a Maxwell-type mechanical model kernel (Maxwell, 1867; Carcione, 2014) and converting the thermal diffusion to wave-like propagation (finite speeds) at high frequencies. The theory predicts two P-waves and an S-wave, the latter not affected by the thermal effects. The P-waves are an elastic wave (E-wave) and a thermal wave (T-wave) having similar characteristics to the fast and slow P-waves of poroelasticity (Biot, 1956). Rudgers (1990) studies the behavior of these waves as a function of frequency. Banerjee and Pao (1974) consider the anisotropic case, studying the behavior of

Manuscript received by the Editor 16 June 2018; revised manuscript received 24 August 2018.
; published online 13 December 2018.

¹Istituto Nazionale di Oceanografia e di Geofisica Sperimentale (OGS), Borgo Grotta Gigante 42c, Sgonico, Trieste 34010, Italy and Hohai University, School of Earth Sciences and Engineering, Nanjing, China.

²Chinese Academy of Sciences, Key Laboratory of Petroleum Resource Research, Institute of Geology and Geophysics, Beijing, China and Chinese Academy of Sciences, Institutions of Earth Sciences, Beijing, China.

³Hohai University, School of Earth Sciences and Engineering, Nanjing, China. E-mail: jba@hhu.edu.cn; baj08@petrochina.com.cn (corresponding author).

⁴La Sapienza University, Department of Physics, Rome, Italy.

⁵China University of Petroleum (East China), School of Geosciences, Qingdao, China. E-mail: lfu@mail.iggcas.ac.cn.

© 2019 Society of Exploration Geophysicists. All rights reserved.

the wavefronts as a function of the propagation direction. The thermoporoelastic case has been studied by Bear et al. (1992) and Sharma (2008).

Ignaczak and Ostoja-Starzewski (2010) study two theories of hyperbolic thermoelasticity, namely, the Lord-Shulman theory (with one relaxation time) and the Green-Lindsay theory (with two relaxation times). The first is basically similar to the equations solved in the present paper (which include the so-called Maxwell-Vernotte-Cattaneo equation), and the second is a generalization by including another (phenomenological) relaxation time in the coupling terms of the stress-strain relations. Recently, Veres et al. (2013) solve the thermoelasticity equations using finite differences based on staggered grids, where the algorithm is applied to model the generation of ultrasound by a laser source in isotropic and transversely isotropic materials.

In this work, we solve the thermoelasticity equations by using the Fourier method to compute the spatial derivatives and an explicit time-integration technique (e.g., Carcione, 2014). To our knowledge, the results presented here are new. The thermoelastic differential equations are of the form $\dot{\mathbf{v}} = \mathbf{M}\mathbf{v}$, where \mathbf{v} is the field vector and \mathbf{M} is the propagation matrix (the dot denotes time differentiation). In the poroelastic case (Carcione and Quiroga-Goode, 1995), all the eigenvalues of \mathbf{M} have a negative real part. The presence of a quasistatic mode (the Biot slow wave) makes the differential equations stiff (Jain, 1984). Although the eigenvalues of the fast waves have a small real part, the eigenvalue of the Biot wave (in the quasistatic regime) has a large real part. Here, we have a similar situation; in addition, the presence of positive real eigenvalues creates instability when using explicit time-integration methods. Carcione and Quiroga-Goode (1995) and Carcione and Seriani (2001) solve the stiff problem by using a splitting or partition method. This method solves both problems (stiffness and instability) by calculating the unstable part of the equations analytically. Snapshots and time histories are obtained by solving the equations of motion with a direct grid algorithm, based on the Fourier pseudospectral method for computing the spatial derivatives and the Runge-Kutta time-integration technique to solve the regular (nonstiff) part of the differential equations. Alternatively, a Crank-Nicolson time-stepping method is also implemented.

As conventional sources of hydrocarbons decline, the exploration is starting to be developed in unexplored or underdeveloped areas. High-pressure-high-temperature (HPHT) reservoirs are increasingly becoming the focus of petroleum exploration in the search for additional reserves. The modeling method developed in this work can be relevant for the exploration of HPHT deep reservoirs and tight oil and gas resources in thermal hydrocarbon source rocks with temperatures greater than 400°C (e.g., Fu, 2012, 2017).

EQUATIONS OF THERMOELASTICITY

Let us define by u_i , $i = 1, 2, 3$ the components of the displacement field, by σ_{ij} the components of the stress tensor and by T the increment of temperature above a reference absolute temperature T_0 for the state of zero stress and strain. In a linear isotropic medium, the stress-strain relations of thermoelasticity are given by Biot (1956, equations 2.2 and 10.1).

Strain-displacement relations

$$\begin{aligned} \epsilon &= \epsilon_{xx} + \epsilon_{yy} + \epsilon_{zz}, \\ \epsilon_{xx} &= \partial_x u_x, \quad \epsilon_{yy} = \partial_y u_y, \quad \epsilon_{zz} = \partial_z u_z, \\ 2\epsilon_{xy} &= \partial_x u_y + \partial_y u_x, \\ 2\epsilon_{xz} &= \partial_x u_z + \partial_z u_x, \\ 2\epsilon_{yz} &= \partial_y u_z + \partial_z u_y, \end{aligned} \quad (1)$$

where ϵ_{ij} denotes the strain components.

Stress-strain relations

$$\begin{aligned} \sigma_{xx} &= 2\mu\epsilon_{xx} + \lambda\epsilon - \beta T + f_{xx}, \\ \sigma_{yy} &= 2\mu\epsilon_{yy} + \lambda\epsilon - \beta T + f_{yy}, \\ \sigma_{zz} &= 2\mu\epsilon_{zz} + \lambda\epsilon - \beta T + f_{zz}, \\ \sigma_{xy} &= 2\mu\epsilon_{xy} + f_{xy}, \\ \sigma_{xz} &= 2\mu\epsilon_{xz} + f_{xz}, \\ \sigma_{yz} &= 2\mu\epsilon_{yz} + f_{yz}, \end{aligned} \quad (2)$$

where λ and μ are the Lamé constants

$$\beta = (3\lambda + 2\mu)\alpha, \quad (3)$$

with α is the coefficient of thermal expansion and f_{ij} are the external stress forces.

Equations of momentum conservation

$$\begin{aligned} \partial_x \sigma_{xx} + \partial_y \sigma_{xy} + \partial_z \sigma_{xz} &= \rho \ddot{u}_x + f_x, \\ \partial_x \sigma_{xy} + \partial_y \sigma_{yy} + \partial_z \sigma_{yz} &= \rho \ddot{u}_y + f_y, \\ \partial_x \sigma_{xz} + \partial_y \sigma_{yz} + \partial_z \sigma_{zz} &= \rho \ddot{u}_z + f_z, \end{aligned} \quad (4)$$

where ρ is the mass density and f_i are the components of external body forces and a dot above a variable denotes time differentiation.

Law of heat conduction

$$\gamma \Delta T = c(\dot{T} + \tau \ddot{T}) + T_0 \beta (\dot{\epsilon} + \tau \ddot{\epsilon}) + q, \quad (5)$$

where γ is the coefficient of heat conduction (or thermal conductivity), c is the specific heat of the unit volume in the absence of deformation, τ is a relaxation time, q is a heat source, and Δ is the Laplacian (Rudgers, 1990). Biot (1956) and Deresiewicz (1957) do not consider the relaxation term, leading to unphysical results.

Substituting the stress-strain relations into the equations of momentum conservation and using the strain-displacement relations, we obtain compact equations for the displacement components and temperature fluctuation

$$\begin{aligned} \mu u_{j,kk} + (\lambda + \mu) u_{k,kj} - \beta T_{,j} &= \rho \ddot{u}_j, \\ \gamma T_{,kk} &= c(\dot{T} + \tau \ddot{T}) + T_0 \beta (\dot{u}_{k,k} + \tau \ddot{u}_{k,k}) + q, \end{aligned} \quad (6)$$

where Einstein implicit summation is assumed. Deresiewicz (1957) equations assume $\tau = 0$ (Fourier's law). We use the notation of this paper because α as given by Biot is three times that of Deresiewicz, whereas Rudgers (1990) defines β as 3α , without the bulk modulus $\lambda + 2\mu/3$.

PLANE-WAVE ANALYSIS

Let us assume that the displacement vector \mathbf{u} , and T can be described by the following plane waves:

$$\mathbf{u} = \mathbf{U} \exp[i\omega(t - \mathbf{s} \cdot \mathbf{x})], T = T_0 \exp[i\omega(t - \mathbf{s} \cdot \mathbf{x})], \quad (7)$$

where ω is the angular frequency, \mathbf{s} is the slowness vector, \mathbf{x} is the position vector, and $i = \sqrt{-1}$. In general $\mathbf{s} = \mathbf{s}_R - i\bar{\alpha}/\omega$, where $\bar{\alpha}$ is the attenuation vector, and the plane wave is termed inhomogeneous because these real and imaginary vectors do not point out in the same direction. Assuming homogeneous fields, we have $\mathbf{s} = s(l_1, l_2, l_3)^\top$, where $s = 1/V_c = s_R - i\bar{\alpha}/\omega$, where V_c is the complex velocity, $\bar{\alpha}$ is the attenuation factor, and l_i are the directions cosines defining the propagation direction. Here, these cosines do not appear in the following calculations because the medium is isotropic.

Dispersion relation and complex velocity

If we consider S-waves, i.e., $U_i l_i = 0$ (the displacement vector is perpendicular to the propagation direction), we obtain, after replacing the plane waves into equation 6, the dispersion relation (Deresiewicz, 1957):

$$\mu k^2 - \rho \omega^2 = 0, \quad (8)$$

where $k = \omega s$ is the complex wavenumber. This gives a phase velocity

$$V_S = \sqrt{\frac{\mu}{\rho}}. \quad (9)$$

Then, S-waves are not affected by the thermal effects, basically because the shear stresses are independent of temperature.

When the displacement vector is pointing in the direction of the wavenumber vector, i.e., when $U_i l_i = 1$, we obtain the dispersion relation for the P-waves, whose complex velocities V_c are solutions of

$$V_c^4 - (V_A^2 + M)V_c^2 + MV_I^2 = 0, \quad M = \frac{i\omega a^2}{1 + i\omega\tau}, \quad (10)$$

where V_I and V_A are the isothermal and adiabatic phase velocities (see Rudgers, 1990), given by, respectively

$$V_I = \sqrt{\frac{\lambda + 2\mu}{\rho}} \quad \text{and} \quad V_A = \sqrt{V_I^2 + b^2}, \quad (11)$$

where M is a complex kernel arising from a Maxwell mechanical model of viscoelasticity (e.g., Carcione, 2014), and

$$a = \sqrt{\frac{\gamma}{c}}, \quad b = \beta \sqrt{\frac{T_0}{\rho c}}, \quad (12)$$

where a is the thermal diffusivity.

Equation 10 has the solutions

$$2V_c^2 = V_A^2 + M \pm \sqrt{(V_A^2 + M)^2 - 4MV_I^2}. \quad (13)$$

There are two P-wave solutions, an elastic E-wave (plus sign) and a thermal T-wave (minus sign). At $\omega = 0$, we have two real solutions:

$$V_c = 0 \text{ (T-wave)}, \quad V_c = V_A \text{ (E-wave)}. \quad (14)$$

For $c \rightarrow \infty$, we obtain $V_c = V_I$, whereas for $\gamma \rightarrow 0$, we have $V_c = V_A$.

Rudgers (1990) takes

$$\tau = \frac{\gamma}{cV_I^2} \quad (15)$$

for his lattice model (see his equations 35, 38, and 58), and we assume this value here to illustrate the theory, giving a relaxation peak at laboratory frequencies for typical rocks as we shall see below. Then, for $\omega \rightarrow \infty$, we have $M \rightarrow a^2/\tau = V_I^2$ and the solution is

$$2V_c^2 = V_A^2 + V_I^2 \pm \sqrt{(V_A^2 + V_I^2)^2 - 4V_I^4}. \quad (16)$$

Because of the choice 15, $\gamma \rightarrow \infty$ and $\omega \rightarrow \infty$ are equivalent. Let us denote the high-frequency limit E- and T-wave velocities, solutions of 16, by $V_{E\infty}$ and $V_{T\infty}$, respectively. Then, $V_{E\infty} > V_A > V_I > V_{T\infty}$.

A range of values of τ yields a superposition of relaxation peaks leading to a general dependence of attenuation with frequency (e.g., Wang and Santamarina, 2007). High and low values of τ correspond to peak locations, f_p at low and high frequencies, respectively, with

$$f_p \approx \frac{1}{2\pi\tau}. \quad (17)$$

Phase velocity, attenuation, and quality factors

The phase velocity and attenuation factor can be obtained from the complex velocity as

$$V_P = [\text{Re}(V_c^{-1})]^{-1} \quad \text{and} \quad A = -\omega \text{Im}(V_c^{-1}), \quad (18)$$

respectively (e.g., Carcione, 2014).

Deresiewicz (1957) introduces the attenuation coefficient as the ratio of the energy dissipated per stress cycle to the total vibrational energy. It is

$$L = 4\pi \cdot \frac{AV_P}{\omega}. \quad (19)$$

2D DIFFERENTIAL EQUATIONS OF MOTION

We consider the 2D case in the (x, z) plane and solve the differential equations by using the first-order time-derivative approach,

called particle velocity-stress formulation in elasticity. Here, it should be called particle velocity-stress-temperature formulation.

Particle velocity-stress-temperature formulation

Denoting the particle-velocity components by V_i , we have from equations 1–5

$$\begin{aligned}\dot{V}_x &= \rho^{-1}(\partial_x \sigma_{xx} + \partial_z \sigma_{xz} - f_x) \equiv \Pi_x, \\ \dot{V}_z &= \rho^{-1}(\partial_x \sigma_{xz} + \partial_z \sigma_{zz} - f_z) \equiv \Pi_z, \\ \dot{\sigma}_{xx} &= 2\mu \dot{\epsilon}_{xx} + \lambda \dot{\epsilon} - \beta \psi + \dot{f}_{xx}, \\ \dot{\sigma}_{zz} &= 2\mu \dot{\epsilon}_{zz} + \lambda \dot{\epsilon} - \beta \psi + \dot{f}_{zz}, \\ \dot{\sigma}_{xz} &= 2\mu \dot{\epsilon}_{xz} + \dot{f}_{xz}, \\ \dot{T} &= \psi, \\ \dot{\psi} &= (c\tau)^{-1}[\gamma \Delta T - q - T_0 \beta (\dot{\epsilon} + \tau(\partial_x \Pi_x + \partial_z \Pi_z))] - \frac{1}{\tau} \psi,\end{aligned}\quad (20)$$

where

$$\begin{aligned}\dot{\epsilon} &= \dot{\epsilon}_{xx} + \dot{\epsilon}_{zz}, \\ \dot{\epsilon}_{xx} &= \partial_x V_x, \quad \dot{\epsilon}_{zz} = \partial_z V_z, \\ 2\dot{\epsilon}_{xz} &= \partial_x V_z + \partial_z V_x, \\ \Delta T &= T_{xx} + T_{zz},\end{aligned}\quad (21)$$

The algorithm

The 2D velocity-stress differential equations can be written in matrix form as

$$\dot{\mathbf{v}} + \mathbf{s} = \mathbf{M}\mathbf{v}, \quad (22)$$

where

$$\mathbf{v} = [V_x, V_z, \sigma_{xx}, \sigma_{zz}, \sigma_{xz}, T, \psi]^T \quad (23)$$

is the unknown array vector

$$\mathbf{s} = [f_x/\rho, f_z/\rho, \dot{f}_{xx}, \dot{f}_{zz}, \dot{f}_{xz}, 0, q']^T \quad (24)$$

is the source vector, and \mathbf{M} is the propagation matrix containing the spatial derivatives and material properties, where $q' = -(c\tau)^{-1}q$.

The solution to equation 22 subject to the initial condition $\mathbf{v}(0) = \mathbf{v}_0$ is formally given by

$$\mathbf{v}(t) = \exp(t\mathbf{M})\mathbf{v}_0 + \int_0^t \exp(\tau\mathbf{M})\mathbf{s}(t-\tau)d\tau, \quad (25)$$

where $\exp(t\mathbf{M})$ is called evolution operator.

The eigenvalues of \mathbf{M} may have negative real parts and differ greatly in magnitude. The presence of large eigenvalues, together with small eigenvalues, indicates that the problem is stiff. Moreover, the presence of real positive eigenvalues can induce instability in the time-stepping method. To solve these problems, the differential equations are solved with the splitting algorithm used by Carcione

and Quiroga-Goode (1995) and Carcione and Seriani (2001). The propagation matrix can be partitioned as

$$\mathbf{M} = \mathbf{M}_r + \mathbf{M}_s, \quad (26)$$

where subscript r indicates the regular matrix, and subscript s denotes the stiff matrix, involving the quantity γ and the coupling terms. The evolution operator can be expressed as $\exp(\mathbf{M}_r + \mathbf{M}_s)t$. It is easy to show that the product formula

$$\exp(\mathbf{M}dt) = \exp\left(\frac{1}{2}\mathbf{M}_s dt\right) \exp(\mathbf{M}_r dt) \exp\left(\frac{1}{2}\mathbf{M}_s dt\right) \quad (27)$$

is second-order accurate in dt . Equation 27 allows us to solve the unstable equations separately. From equation 20, these are

$$\begin{aligned}\dot{\sigma}_{xx} &= -\beta\psi, \\ \dot{\sigma}_{zz} &= -\beta\psi, \\ \dot{\psi} &= -\frac{1}{\tau}\psi = -\frac{cV_1^2}{\gamma}\psi,\end{aligned}\quad (28)$$

where \mathbf{M}_s has only these elements different from zero: $\mathbf{M}_{s37} = -\beta$, $\mathbf{M}_{s47} = -\beta$, and $\mathbf{M}_{s77} = -1/\tau$.

Let us discretize the time variable as $t = ndt$, where dt is the time step, and denote with a superscript “*” the intermediate fields to obtain the solution at $(n+1)dt$ fields from fields at ndt . Equation 28 has the solution

$$\begin{aligned}\sigma_{xx}^* &= \sigma_{xx}^n + \tau\beta[\exp(-dt/\tau) - 1]\psi^n, \\ \sigma_{zz}^* &= \sigma_{zz}^n + \tau\beta[\exp(-dt/\tau) - 1]\psi^n, \\ \psi^* &= \exp(-dt/\tau)\psi^n.\end{aligned}\quad (29)$$

The regular operator $\exp(\mathbf{M}_r dt)$ is approximated with a fourth-order Runge-Kutta solver. The output vector is

$$\mathbf{v}^{n+1} = \mathbf{v}^* + \frac{dt}{6}(\Delta_1 + 2\Delta_2 + 2\Delta_3 + \Delta_4), \quad (30)$$

where

$$\begin{aligned}\Delta_1 &= \mathbf{M}_r \mathbf{v}^* + \mathbf{s}^n, \\ \Delta_2 &= \mathbf{M}_r (\mathbf{v}^* + \frac{dt}{2} \Delta_1) + \mathbf{s}^{n+1/2}, \\ \Delta_3 &= \mathbf{M}_r (\mathbf{v}^* + \frac{dt}{2} \Delta_2) + \mathbf{s}^{n+1/2}, \\ \Delta_4 &= \mathbf{M}_r (\mathbf{v}^* + dt \Delta_3) + \mathbf{s}^{n+1},\end{aligned}\quad (31)$$

and \mathbf{v}^* is the intermediate output vector obtained after the operation with the stiff evolution operator. Then, \mathbf{v}^* is input to a Runge-Kutta fourth-order time-stepping algorithm (involving matrix \mathbf{M}_r), and the spatial derivatives are calculated with the Fourier method by using the FFT (Carcione, 2014). This spatial approximation is infinitely accurate for band-limited periodic functions with cutoff spatial wavenumbers, which are smaller than the cutoff wavenumbers of the mesh. Due to the splitting algorithm, the modeling is second-order accurate in the time discretization.

We give here an alternative time-integration method based on the Crank-Nicolson scheme (see Appendix B). Although it has a first-order accuracy in time, it is more stable than the previous technique for low values of γ .

PHYSICS AND SIMULATIONS

We consider the following reference properties:

$$\begin{aligned}
 &\text{density, } \rho: 2650 \text{ kg/m}^3 \\
 &\text{specific heat, } c: 117 \text{ kg/(m s}^2\text{°K)} \\
 &\text{thermal conductivity, } \gamma: 10.5 \text{ m kg/(s}^3\text{°K)} \\
 &\text{coefficient of thermal expansion, } \alpha: 0.33 \times 10^{-5} \text{°K}^{-1} \\
 &\text{P-wave velocity, } V_1 = \sqrt{(\lambda + 2\mu)/\rho}: 2457 \text{ m/s} \\
 &\text{S-wave velocity, } V_S = \sqrt{\mu/\rho}: 1505 \text{ m/s} \\
 &\text{absolute temperature, } T_0: 300 \text{°K,} \\
 &\text{relaxation time, } \tau = \gamma/(cV_1^2): 1.49 \times 10^{-8} \text{ s,} \quad (32)
 \end{aligned}$$

where we have expressed the quantities in the international systems of units (SI). These values yield

$$\begin{aligned}
 a^2 &= 0.0897 \text{ m}^2/\text{s,} \\
 b &= 2464 \text{ m/s,} \\
 \beta &= 79200 \text{ kg/(m s}^2\text{°K)}. \quad (33)
 \end{aligned}$$

With the choice of τ above, $M \rightarrow V_1^2$ for $\omega \rightarrow \infty$ (see equation 10).

Figures 1 and 2 show the phase velocities of the elastic (E) and thermal (T) waves as a function of frequency for two values of γ . The inflexion point in the E -wave velocity occurs at a frequency of approximately $f_p = V_1^2/(2\pi a^2)$, at nearly 20 MHz in the first case and 50 Hz in the second case. As can be seen, the E -wave low-frequency velocity is the adiabatic one, i.e., $V_A = 3480$ m/s, whereas the isothermal velocity ($V_1 = 2457$ m/s) is not involved in the coupled case. The high-frequency limit velocity is $V_{E\infty} = 3980$ m/s. We can see that in both cases, the attenuation coefficient of the E -wave has a peak with $L \approx 1$. From equation 19, this corresponds to an attenuation factor $A = 2f/V_p$, where f is the frequency. Because $Q \approx \pi f/(V_p A)$, we obtain a peak quality factor $Q = \pi/2$, a very strong attenuation. The location of the relaxation peak depends on the values of γ and τ . Because here γ and τ are related by equation 15, we obtain a peak at the ultrasonic band for values of γ typical of rocks. Increasing τ , the peak moves to low frequencies. The time scale for heat diffusion is a function of the length scale involved in the process of heat flow.

The behavior of the two P-waves is similar to that of the fast and slow P-waves in poroelasticity (e.g., Carcione, 2014). As the slow P-wave, the T -wave is diffusive at low frequencies. In Biot's theory, it is the fluid viscosity/permeability ratio to determine this behavior, whereas here, it is the value of the thermal conductivity/specific heat ratio ($a^2 = \gamma/c$), mainly the value of γ (if $c \rightarrow 0$, $M \rightarrow V_1^2$, $b \rightarrow \infty$, and $V_c \rightarrow \infty$; $c \rightarrow \infty$ yields $V_c = V_1$). Zero viscosity and infinite thermal conductivity yield the same effect, i.e., a wave-like slow wave, as can be seen in the following analysis.

The thermal conductivity γ ranges from 24,000 kg/(s³°K) for CRC aluminum to 0.023 kg/(s³°K) for air, whereas rocks filled with fluids have a range between 1 and 12 m kg/(s³°K). The unre-

alistic values assumed here are intended for a better illustration of the physics. Figure 3 shows the phase velocity (Figure 3a) and attenuation coefficient (Figure 3b) as a function of frequency for two extremes values of γ . As can be seen, for small γ , the T -wave is diffusive, whereas for high γ , the T -wave propagates with a velocity of approximately $V_{T\infty} \approx 1500$ m/s, close to the S -wave velocity. The attenuation levels are the same for both values of γ , which

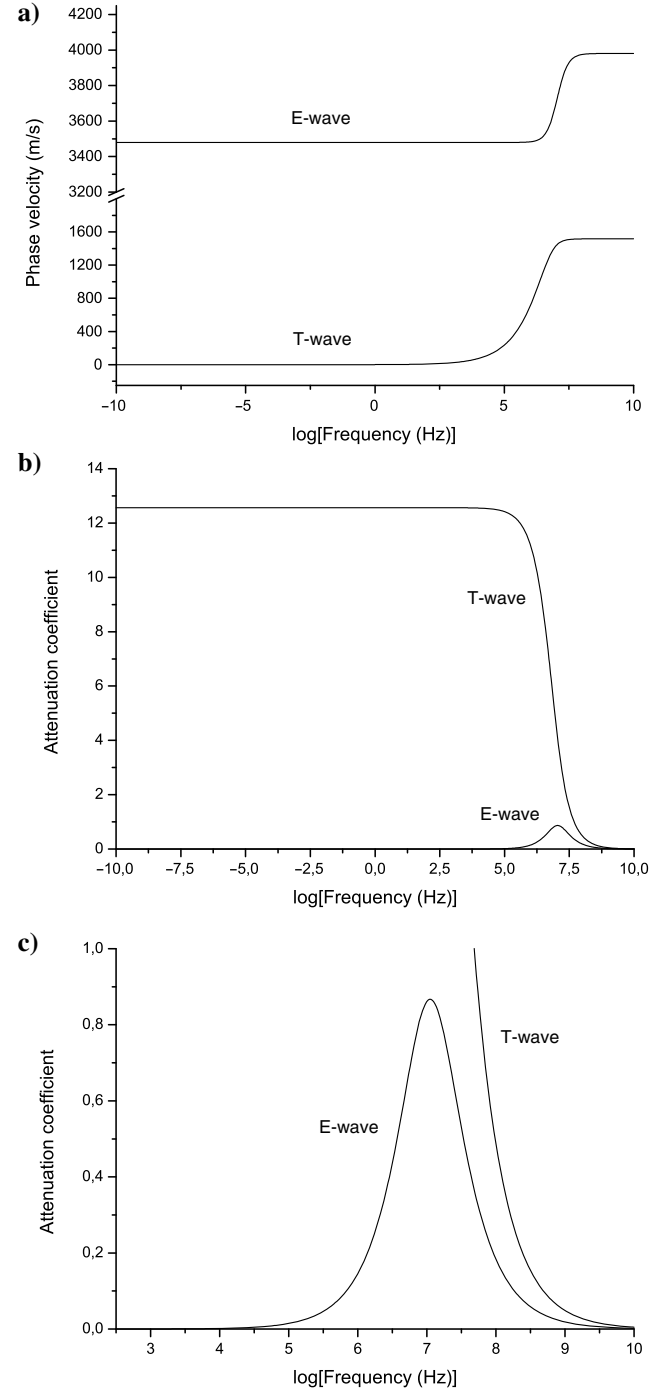


Figure 1. (a) Phase velocity and (b and c) attenuation coefficient as a function of frequency for $\gamma = 10.5 \text{ m kg/(s}^3\text{°K)}$. The attenuation peaks at tens of MHz.

affects the location of the E-wave relaxation peak, as well as the attenuation (step-like) of the T-wave. At the two limits, i.e., $\gamma = 0$, we have $V_c = V_A$ (E-wave) and $V_c = 0$ (T-wave), and for $\gamma = \infty$, we get $M = V_I^2$ and

$$2V_c^2 = V_A^2 + V_I^2 \pm \sqrt{(V_A^2 + V_I^2)^2 - 4V_I^4} = 2V_I^2 + b^2 \pm b\sqrt{b^2 + 4V_I^2}; \quad (34)$$

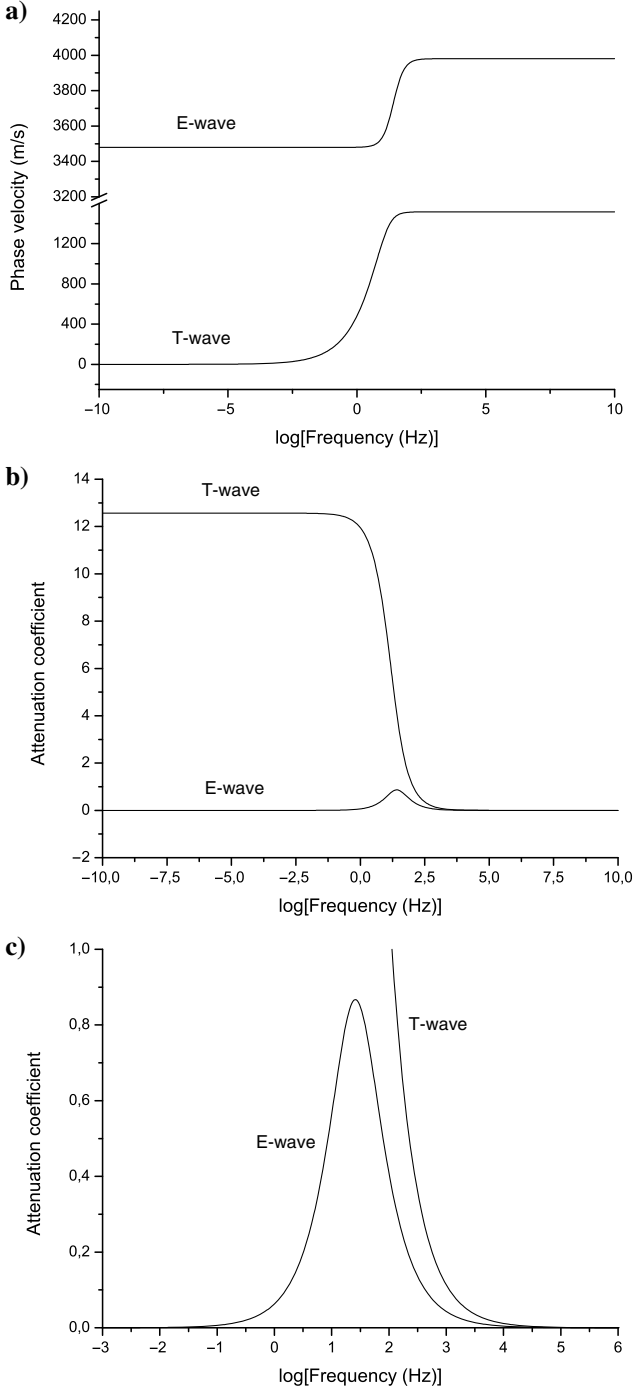


Figure 2. (a) Phase velocity and (b and c) attenuation coefficient as a function of frequency for $\gamma = 4.5 \times 10^6 \text{ m kg}/(\text{s}^3\text{K})$. The attenuation peaks at the seismic band.

i.e., two finite velocities as can be seen in Figure 3a for the high value of γ (blue and green curves), $V_{E\infty} = 3980 \text{ m/s}$ and $V_{T\infty} = 1517 \text{ m/s}$, respectively (the adiabatic E-wave velocity is $V_A = 3480 \text{ m/s}$).

We obtain the eigenvalues of the propagation matrix \mathbf{M} in Appendix A, where we consider the 1D acoustic case. In order that the system of equations is stable, the eigenvalues must be located in the negative $i\omega_c$ plane. For the γ values considered in Figures 1 and 2, the eigenvalue of equation A-4, $\eta = -16 \times 10^6 \text{ s}^{-1}$ ($\gamma = 10.5 \text{ m kg}/(\text{s}^3\text{K})$) and $\eta = -157 \text{ s}^{-1}$ ($\gamma = 1.13 \times 10^6 \text{ m kg}/(\text{s}^3\text{K})$), respectively, for a wavenumber $\kappa = 0$. When $\kappa = \pi/dx$, $dx = 0.1 \text{ mm}$, the results are shown in Figure 4 for both cases. The real positive eigenvalues imply instability when using explicit time-integration methods, such as the Runge-Kutta technique, but these eigenvalues are handled by the time-splitting method. To have numerical stability, the domain of convergence of the time-stepping method should include the real negative eigenvalues. The explicit fourth-order Runge-Kutta method requires $\eta dt < 2.78$. For $dt = 10 \text{ ns}$, use below in the simulations, $\eta < 278 \times 10^6 / \text{s} = 278 (2\pi \text{ MHz})$.

We compute snapshots of the wavefield, where we consider a 231×231 mesh, with square cells and a grid spacing of $dx = dz = 0.1 \text{ mm}$ (a sample of $2.3 \times 2.3 \text{ cm}$). The source is a vertical force located at the center of the mesh and has the time history

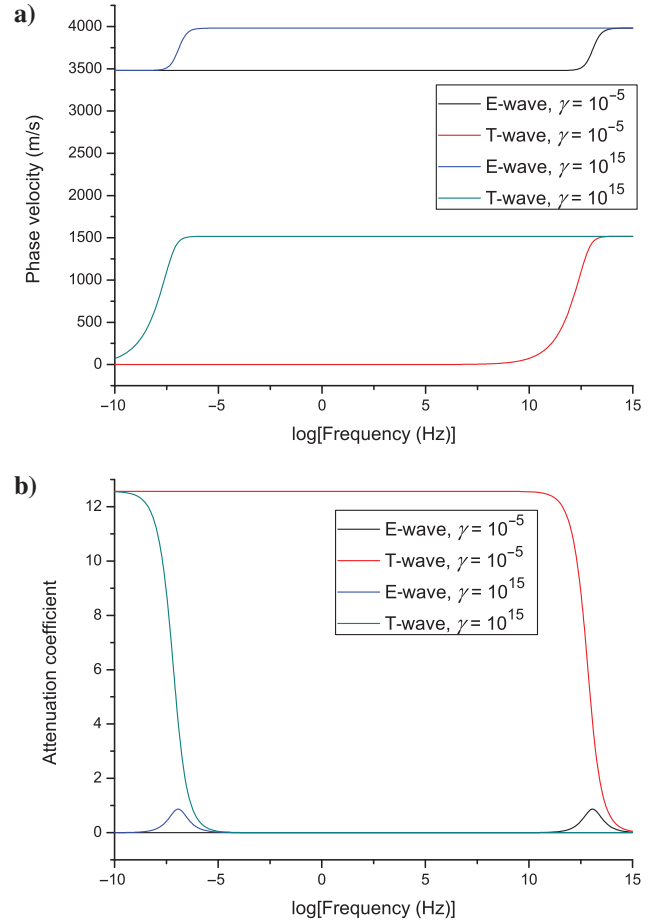


Figure 3. (a) Phase velocity and (b) attenuation coefficient as a function of frequency for two extremes values of γ , given in $\text{m kg}/(\text{s}^3\text{K})$.

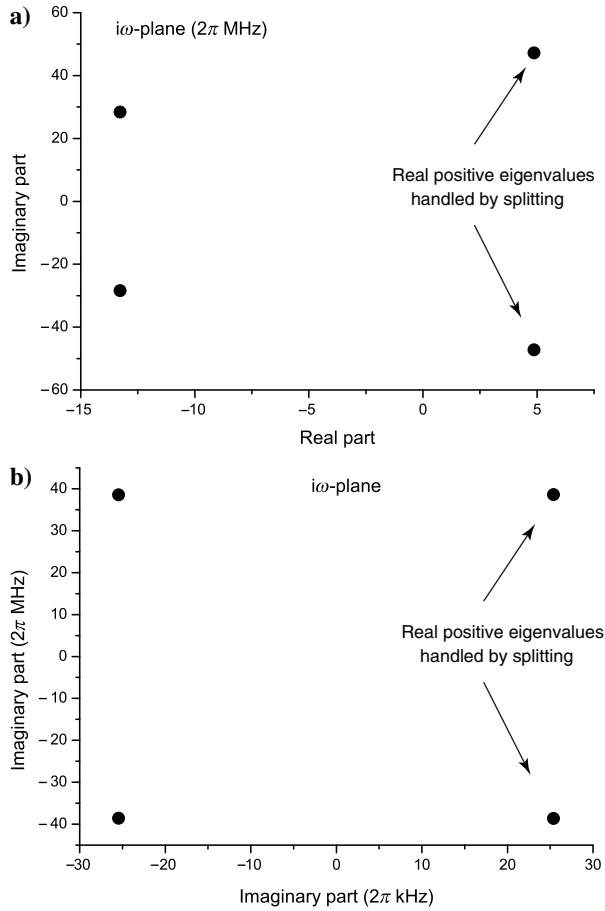


Figure 4. Eigenvalues of the propagation matrix \mathbf{M} in the $i\omega_c$ plane for $\kappa = \pi/dx$, with $dx = 0.1$ mm. (a and b) correspond to the cases in Figures 1 and 2, respectively, with $\mu = 0$. The phase velocities and real frequencies are as follows: (a) $V_P = \pm 1502$ m/s and $f = 7.5$ MHz; $V_P = 905$ m/s and $f = 4.5$ MHz; (b) $V_P = \pm 1230$ m/s and $f = 6.15$ MHz; $V_P = \pm 1228$ m/s and $f = 6.14$ MHz.

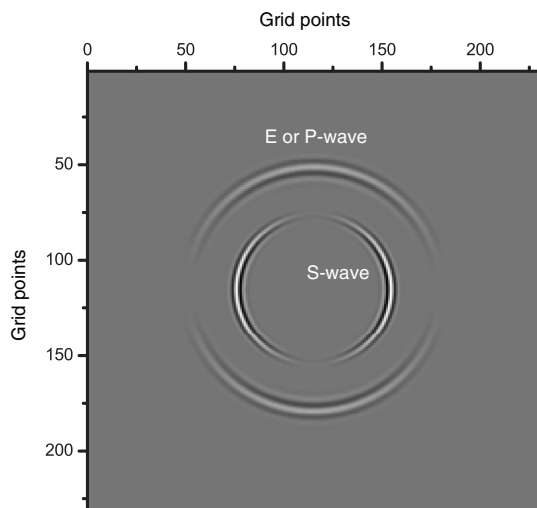


Figure 5. Snapshots of the vertical component of the particle velocity at $3 \mu\text{s}$, corresponding to the uncoupled case. The source is a vertical elastic force of central frequency 3.5 MHz. The P wavefront travels with the isothermal velocity V_I .

$$h(t) = \cos[(t - t_0)f_0] \exp[-2(t - t_0)^2 f_0^2], \quad (35)$$

where $f_0 = 3.5$ MHz is the central frequency and $t_0 = 3/(2f_0)$ is a delay time. The time step of the Runge-Kutta algorithm is $dt = 10$ ns. Figure 5 shows the snapshot of the vertical component of the particle velocity at $3 \mu\text{s}$, corresponding to the uncoupled case ($\alpha = 0$). The source is a vertical force f_z . The P- and S-waves can be seen, with the P wavefront traveling with the isothermal velocity V_I .

Figures 6 and 7 show the vertical particle velocity (a) and temperature field (b) for a heat source and $\gamma = 10.5$ m kg/(s³K) and $\gamma = 1.13 \times 10^6$ m kg/(s³K), respectively. No S-wave is present as expected. The velocity of the E-wave in Figure 6 is slightly less than $V_{E\infty}$, according to Figure 1a (the source central frequency is 3.5 MHz, i.e., 6.5 in abscissa). In Figure 7, the velocities of the

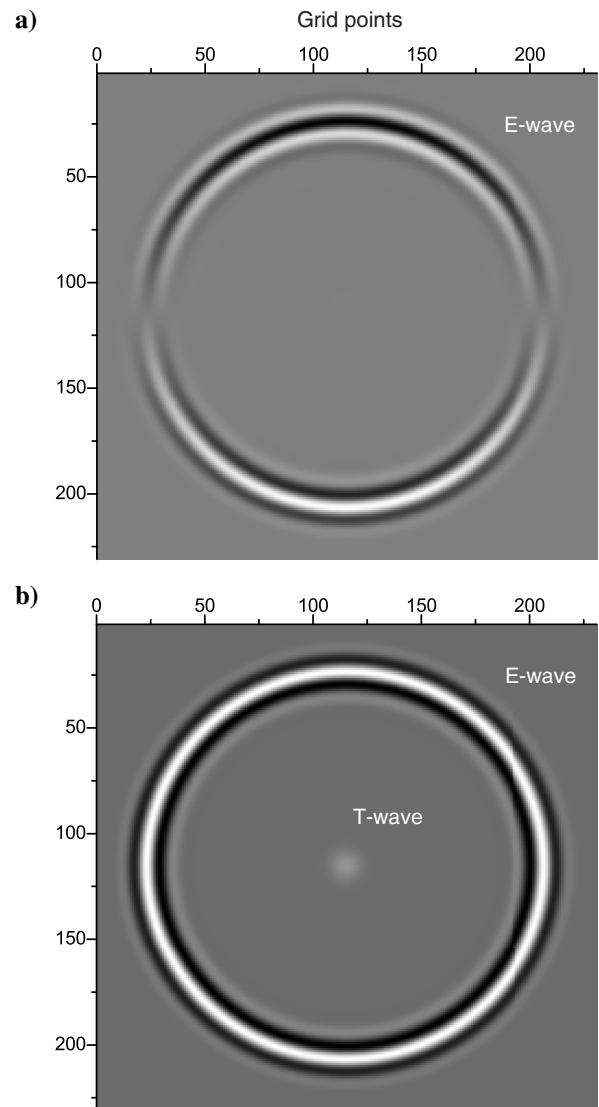


Figure 6. Snapshots of the vertical component of the (a) particle velocity and (b) temperature at $3 \mu\text{s}$, corresponding to the coupled case with $\gamma = 10.5$ m kg/(s³K). The perturbation is a heat source q , with a central frequency of 3.5 MHz. The E wavefront travels with a velocity between V_A and $V_{E\infty}$.

E- and T-waves are $V_{E\infty}$ and $V_{T\infty}$, respectively. The T-wave is diffusive in Figure 6 because it is highly attenuated, according to the curves of Figure 1b, whereas the attenuation is negligible in Figure 7, in agreement with the attenuation curve of Figure 2b.

Figure 8 shows the vertical particle velocity (Figure 8a) and temperature field (Figure 8b) for a vertical force and $\gamma = 10.5 \text{ m kg}/(\text{s}^3\text{K})$, where the fields are enhanced, compared with the previous plots, to highlight the wave modes. In this case, the S-wave is generated but the T-wave (or diffusive mode) is not so strong as that generated by the heat source (see Figure 6).

Next, we compute fields in the seismic band by using a Crank-Nicolson scheme (see Appendix B). We consider a 231×231 mesh, with square cells and a grid spacing of $dx = dz = 10 \text{ m}$ ($2.31 \times 2.31 \text{ km}$). The source is dilatational ($f_{xx} = f_{zz}$) located at the center of the mesh with $f_0 = 25 \text{ Hz}$. The time step is $dt = 1 \text{ ms}$.

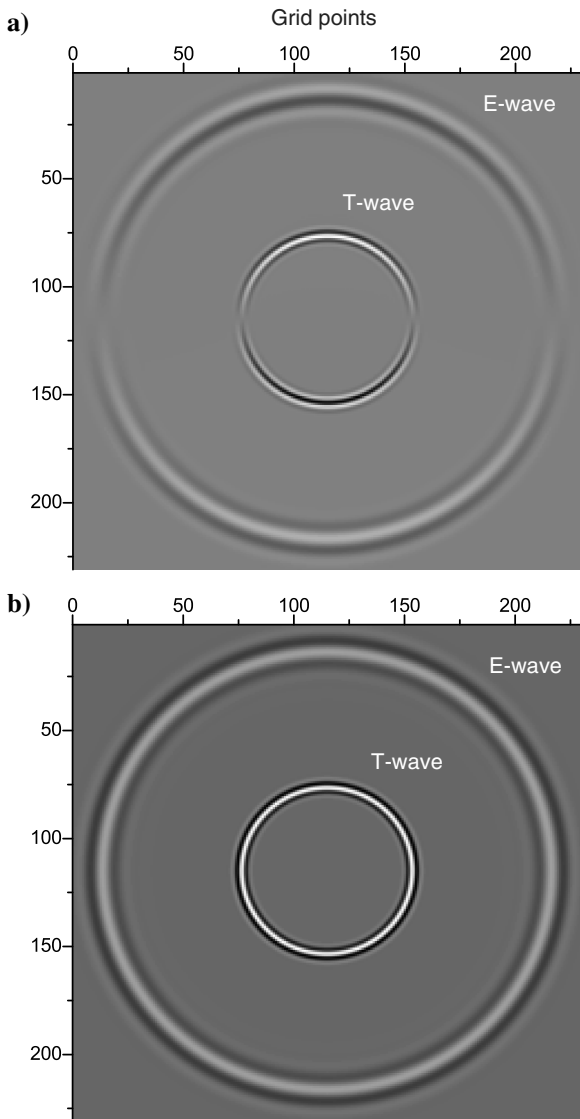


Figure 7. Snapshots of the vertical component of the (a) particle velocity and (b) temperature at $3 \mu\text{s}$, corresponding to the coupled case with $\gamma = 4.5 \times 10^6 \text{ m kg}/(\text{s}^3\text{K})$. The perturbation is a heat source q , with a central frequency of 3.5 MHz . The E and T wavefronts travel with the velocities $V_{E\infty}$ and $V_{T\infty}$, respectively.

Figure 9 shows snapshots of the vertical component of the particle velocity at 0.3 s , corresponding to the uncoupled (Figure 9a) ($\alpha = 0$) and coupled (Figure 9b and 9c) cases. In Figure 9a, the E wavefront travels with the isothermal velocity $V_I = 2457 \text{ m/s}$. In Figure 9b and 9c, the velocities are $V_A = 3480 \text{ m/s}$ (adiabatic) and $V_{E\infty} = 3980 \text{ m/s}$ (high-frequency limit), corresponding to low and high values of the thermal conductivity γ . The T-wave travels with the velocity, $V_{T\infty}$ indicated in Figure 3a (green line).

Finally, we present an example of inhomogeneous model. A plane interface separates two half spaces. The upper medium has $\gamma = 4.5 \times 10^7 \text{ m kg}/(\text{s}^3\text{K})$ and the P and S used for the previous simulations, whereas the lower medium has $\gamma = 10.5 \text{ m kg}/(\text{s}^3\text{K})$, $V_P = 3200 \text{ m/s}$, and $V_S = 1800 \text{ m/s}$. The other properties are the same for both half-spaces. Figure 10 shows the snapshots of the vertical component of the particle velocity (Figure 10a) and temper-

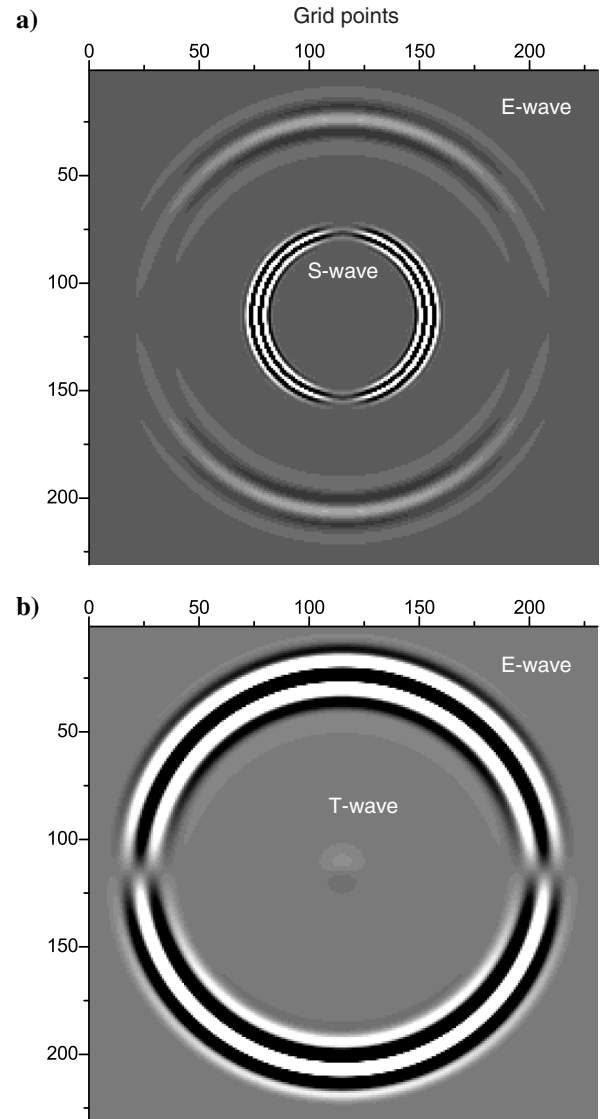


Figure 8. Snapshots of the vertical component of the (a) particle velocity and (b) temperature at $3 \mu\text{s}$, corresponding to the coupled case with $\gamma = 10.5 \text{ m kg}/(\text{s}^3\text{K})$. The source is a vertical elastic force of central frequency 3.5 MHz . The S-wave is uncoupled with the temperature field.

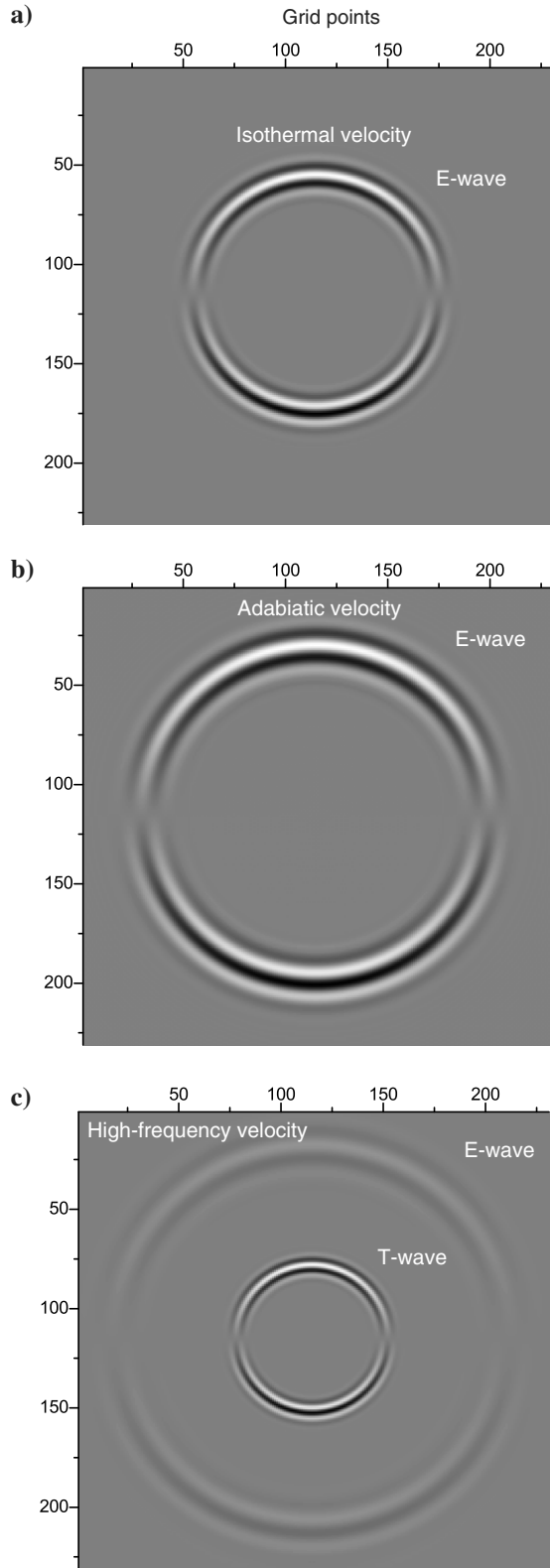


Figure 9. Snapshots of the vertical component of the particle velocity at 0.3 s, corresponding to the (a) uncoupled case ($\alpha = 0$), (b) $\gamma = 10.5 \text{ m kg}/(\text{s}^3\text{K})$, and (c) $\gamma = 10^{15} \text{ m kg}/(\text{s}^3\text{K})$. The source is a dilatational perturbation of central frequency 50 Hz (seismic band).

ature field (Figure 10b) at the 0.3 s propagation time, such that the wave does not cross the boundary and absorbing strips are not needed. The perturbation is a heat source, indicated by a star, with a central frequency of 70 Hz. S-waves are decoupled and should not be present in Figure 10b. A tentative interpretation of the different events is as follows: RP, reflected P wave; RTP, reflected T-wave and converted to P; TrT, transmitted T-wave; TrTP, transmitted T-wave converted to P; TrP, transmitted P-wave; and RT, reflected T-wave. Head (lateral) waves with a planar wavefront can also be observed. Even if the heterogeneity is a simple plane interface, the wavefield is complex and could be more complex in the presence of significant S waves, generated, for instance, by a vertical elastic force.

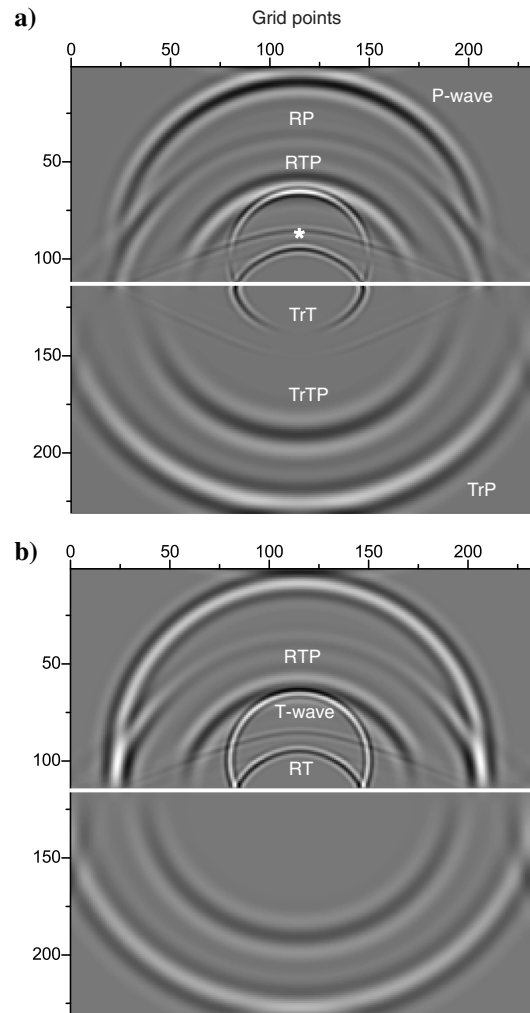


Figure 10. Inhomogeneous model. Snapshots of the vertical component of the (a) particle velocity and (b) temperature field at 0.3 s propagation time. The horizontal interface separates the two half spaces of dissimilar properties. The upper medium has $\gamma = 4.5 \times 10^7 \text{ m kg}/(\text{s}^3\text{K})$ (T-wave wave-like) and the P and S used for the previous simulations, whereas the lower medium has higher velocities and $\gamma = 10.5 \text{ m kg}/(\text{s}^3\text{K})$ (T-wave diffusive). The other properties are similar. The perturbation is a heat source, indicated by a star, with a central frequency of 70 Hz. Direct, reflected (R), and transmitted (Tr) waves can be observed. The P-wave has to be identified with the E-wave.

CONCLUSION

We have proposed a numerical algorithm to solve the differential equations of thermoelasticity, i.e., coupling elasticity with thermal effects. The modeling is a direct-grid method that allows us to handle spatially inhomogeneous media. It is based on the Fourier method to compute the spatial derivatives and a Runge-Kutta time-stepping technique combined with a splitting method to compute the time evolution of the wavefield. The splitting or partition method solves a numerical instability problem. Another time-stepping method, based on a Crank-Nicolson scheme, provides an alternative solution for verification of the numerical solution.

Three waves propagate: the E-wave (or fast P-wave), a thermal P-wave/diffusion (T-wave), and the S-wave. The first two are coupled, and thermal effects induce elastic dissipation of the E-wave. At low frequencies, the T-wave is a diffusive mode. The physics of wave propagation is analyzed in detail for several values of the properties, and the velocities of the different wave modes are precisely determined under different conditions. The simulations show the complexity of the wavefield, which can be interpreted after a detailed study of the physics. The location of thermoelastic relaxation peak describing the attenuation in the frequency axis depends on the diffusion length of the heat flow. Future research involves the generalization of the proposed modeling algorithm to the anisotropic and poroelastic cases.

ACKNOWLEDGMENTS

This work is supported by the Strategic Priority Research Program of the Chinese Academy of Sciences, Grant No. XDA14010303, Major State Research Development Program of China under Grant No. 2016YFC0601101, the Specially-Appointed Professor Program of Jiangsu Province, China, and the Cultivation Program of “111” Plan of China (BC2018019).

DATA AND MATERIALS AVAILABILITY

Data associated with this research are available and can be obtained by contacting the corresponding author.

APPENDIX A

EIGENVALUES OF THE PROPAGATION MATRIX

To study the eigenvalues of \mathbf{M} (equation 22), we set $\mu = 0$ because the S-wave is not affected by the thermal effects, and we consider the 1D case. Let V and σ denote the particle velocity and stress, respectively. From equation 20, we obtain

$$\begin{aligned}\dot{V} &= \rho^{-1} \partial_x \sigma, \\ \dot{\sigma} &= \lambda \partial_x V - \beta \psi, \\ \dot{T} &= \psi, \\ \dot{\psi} &= (c\tau)^{-1} [\gamma \partial_{xx} T - T_0 \beta (\partial_x V + \tau \rho^{-1} \partial_{xx} \sigma)] - \frac{1}{\tau} \psi, \\ &= V_1^2 \partial_{xx} T - \frac{V_1^2}{\gamma} (\beta T_0 \partial_x V + c\psi) - \frac{\beta T_0}{\rho c V_1^2} \partial_{xx} \sigma, \quad (\text{A-1})\end{aligned}$$

using equation 15, where $V_1 = \sqrt{\lambda/\rho}$ and $\beta = 3\lambda\alpha$. The field vector becomes $\mathbf{v} = [V, \sigma, T, \psi]^T$, and let us consider a plane wave

$$\mathbf{v} = \mathbf{v}_0 \exp[i(\omega_c t - \kappa x)], \quad (\text{A-2})$$

where ω_c is the complex frequency and κ is the real wavenumber. Equation 22 gives an eigenvalue equation for the eigenvalue $\eta = i\omega_c$, to solve for the determinant of the matrix

$$\mathbf{M} - \eta \mathbf{I}_4 = \begin{pmatrix} -\eta & -i\rho^{-1}\kappa & 0 & 0 \\ -i\lambda\kappa & -\eta & 0 & -\beta \\ 0 & 0 & -\eta & 1 \\ \frac{iV_1^2\beta T_0}{\gamma}\kappa & \frac{\beta T_0}{\rho c V_1^2}\kappa^2 & -V_1^2\kappa^2 & -\frac{cV_1^2}{\gamma} - \eta \end{pmatrix}, \quad (\text{A-3})$$

where \mathbf{I}_4 is the 4×4 identity matrix. The numerical discretization uses wavenumbers from 0 to π/dx (the Nyquist wavenumber), where dx is the grid spacing. For $\kappa = 0$, there are three eigenvalues equal to zero and

$$\eta = -\frac{cV_1^2}{\gamma} = -\frac{1}{\tau}. \quad (\text{A-4})$$

The complex velocity is

$$V_c = \frac{\omega_c}{\kappa}. \quad (\text{A-5})$$

According to Carcione (2014), the phase velocity is

$$V_P = \text{Re}(V_c) \quad (\text{A-6})$$

and $\omega = \text{Re}(\omega_c)$.

APPENDIX B

CRANK-NICOLSON EXPLICIT SCHEME

The Crank-Nicolson explicit scheme has been used by Carcione and Quiroga-Goode (1995) to solve the equations of poroelasticity. The scheme, adapted to the thermoelasticity equations, is

$$\begin{aligned}D^{1/2}V_x &= \rho^{-1}(\partial_x \sigma_{xx}^n + \partial_z \sigma_{xz}^n - f_x^n) = \Pi_x^n, \\ D^{1/2}V_z &= \rho^{-1}(\partial_x \sigma_{xz}^n + \partial_z \sigma_{zz}^n - f_z^n) = \Pi_z^n, \\ \dot{\epsilon} &= \partial_x A^{1/2}V_x + \partial_z A^{1/2}V_z, \\ \ddot{\epsilon} &= \partial_x \Pi_x^n + \partial_z \Pi_z^n, \\ \gamma \Delta T^n &= c(A^{1/2}\psi + \tau D^{1/2}\psi) + T_0 \beta (\dot{\epsilon} + \tau \ddot{\epsilon}) + q^n, \\ T^{n+1} &= T^n + dt \psi^{n+1/2}, \\ D^1 \sigma_{xx} &= 2\mu \partial_x A^{1/2}V_x + \lambda \dot{\epsilon} - \beta A^{1/2}\psi, \\ D^1 \sigma_{zz} &= 2\mu \partial_z A^{1/2}V_z + \lambda \dot{\epsilon} - \beta A^{1/2}\psi, \\ D^1 \sigma_{xz} &= 2\mu (\partial_z A^{1/2}V_x + \partial_x A^{1/2}V_z), \quad (\text{B-1})\end{aligned}$$

where

$$D^j \phi = \frac{\phi^{n+j} - \phi^{n-j}}{2j dt} \quad \text{and} \quad A^j \phi = \frac{\phi^{n+j} + \phi^{n-j}}{2}, \quad (\text{B-2})$$

are the central differences and mean value operators, based on a Crank-Nicolson (staggered) implicit scheme (Jain, 1984, p. 269) for

the particle velocities. In this three-level scheme, (V_x, V_z, ψ) at time $(n + 1/2)dt$ and stresses and temperature at time $(n + 1)dt$ are computed explicitly from (V_x, V_z, ψ) at time $(n - 1/2)dt$ and stresses and temperature at time $(n - 1)dt$ and ndt , respectively.

The fifth equation of equation B-1 yields

$$(dt + 2\tau)\psi^{n+1/2} = \frac{2dt}{c} [\gamma\Delta T^n - T_0\beta(\dot{\epsilon} + \tau\ddot{\epsilon}) + q^n] - (dt - 2\tau)\psi^{n-1/2}. \quad (\text{B-3})$$

The stability analysis has been performed in [Carcione and Quiroga-Goode \(1995\)](#), i.e., a Von Neumann stability analysis based on the eigenvalues of the amplification matrix ([Jain, 1984](#), p. 418). The algorithm has first-order accuracy, but it possesses the stability properties of implicit algorithms, and the solution can be obtained explicitly.

REFERENCES

- Armstrong, B. H., 1984, Models for thermoelastic in heterogeneous solids attenuation of waves: *Geophysics*, **49**, 1032–1040, doi: [10.1190/1.1441718](#).
- Banerjee, D. K., and Y.-H. Pao, 1974, Thermoelastic waves in anisotropic solids: *Journal of Acoustical Society of America*, **56**, 1444–1454, doi: [10.1121/1.1903463](#).
- Bear, J., S. Sorek, G. Ben-Dor, and G. Mazor, 1992, Displacement waves in saturated thermoelastic porous media. I: Basic equations: *Fluid Dynamics Research*, **9**, 155–164, doi: [10.1016/0169-5983\(92\)90002-E](#).
- Biot, M. A., 1956, Thermoelasticity and irreversible thermodynamics: *Journal of Applied Physics*, **27**, 240–253, doi: [10.1063/1.1722351](#).
- Boschi, E., 1973, A thermoviscoelastic model of the earthquake source mechanism: *Journal of Geophysical Research*, **78**, 7733–7737, doi: [10.1029/JB078i032p07733](#).
- Carcione, J. M., 2014, *Wave fields in real media: Theory and numerical simulation of wave propagation in anisotropic, anelastic, porous and electromagnetic media*, 3rd ed.: Elsevier.
- Carcione, J. M., and G. Quiroga-Goode, 1995, Some aspects of the physics and numerical modeling of Biot compressional waves: *Journal of Computational Acoustics*, **3**, 261–280, doi: [10.1142/S0218396X95000136](#).
- Carcione, J. M., and G. Seriani, 2001, Wave simulation in frozen porous media: *Journal of Computational Physics*, **170**, 676–695, doi: [10.1006/jcph.2001.6756](#).
- Cattaneo, C., 1958, Sur une forme de l'équation de la chaleur éliminant paradoxe d'une propagation instantanée: *Comptes rendus de l'Académie des Sciences*, **247**, 431–433.
- Deresiewicz, H., 1957, Plane waves in a thermoelastic solid: *Journal of the Acoustical Society of America*, **29**, 204–209, doi: [10.1121/1.1908832](#).
- Fu, L.-Y., 2012, Evaluation of sweet spot and geopressure in Xihu, Sag. Tech. Report, CCL2012-SHPS-0018ADM: Key Laboratory of Petroleum Resource Research, Institute of Geology and Geophysics, Chinese Academy of Sciences.
- Fu, L.-Y., 2017, Deep-superdeep oil & gas geophysical exploration 111, Program report jointly initiated by MOE and SAFEA, B18055: School of Geosciences, China University of Petroleum (East China).
- Ignaczak, J., and M. Ostoja-Starzewski, 2010, *Thermoelasticity with finite wave speeds*: Oxford Science Publications.
- Jacquey, A. B., M. Cacace, G. Blöcher, and M. Scheck-Wenderoth, 2015, Numerical investigation of thermoelastic effects on fault slip tendency during injection and production of geothermal fluids: *Energy Procedia*, **76**, 311–320, doi: [10.1016/j.egypro.2015.07.868](#).
- Jain, M. K., 1984, *Numerical solutions of partial differential equations*: Wiley Eastern Ltd.
- Maxwell, J. C., 1867, On the dynamic theory of gases: *Philosophical Transactions of the Royal Society A*, **157**, 49–88, doi: [10.1098/rstl.1867.0004](#).
- Rudgers, A. J., 1990, Analysis of thermoacoustic wave propagation in elastic media: *Journal of the Acoustical Society of America*, **88**, 1078–1094, doi: [10.1121/1.399856](#).
- Savage, J., 1966, Thermoelastic attenuation of elastic waves by cracks: *Journal of Geophysical Research*, **71**, 3929–3938, doi: [10.1029/JZ071i016p03929](#).
- Sharma, M. D., 2008, Wave propagation in thermoelastic saturated porous medium: *Journal of Earth System Science*, **117**, 951–958, doi: [10.1007/s12040-008-0080-4](#).
- Treitel, S., 1959, On the attenuation of small-amplitude plane stress waves in a thermoelastic solid: *Journal of Geophysical Research*, **64**, 661–665, doi: [10.1029/JZ064i006p00661](#).
- Veres, I. A., T. Berer, and P. Burgholzer, 2013, Numerical modeling of thermoelastic generation of ultrasound by laser irradiation in the coupled thermoelasticity: *Ultrasonics*, **53**, 141–149, doi: [10.1016/j.ultras.2012.05.001](#).
- Vernotte, P., 1948, Théorie continue et théorie moléculaire des phénomènes thermocinétiques: *Comptes rendus de l'Académie des Sciences*, **227**, 43–44.
- Wang, Y.-H., and J. C. Santamarina, 2007, Attenuation in sand: An exploratory study on the small-strain behavior and the influence of moisture condensation: *Granular Matter*, **9**, 365–376, doi: [10.1007/s10035-007-0050-6](#).
- Zener, C., 1938, Internal friction in solids. II: General theory of thermoelastic internal friction: *Physical Review*, **53**, 90–99, doi: [10.1103/PhysRev.53.90](#).